Influence of Load Modes on the Characteristics of Severe Plastic Deformation Based on Crystal Plasticity Finite Element Method

Jinghui Li, Renhai Yu, Jintong Chen, Fuguo Li, Shan Liang, and Mingya Zhang

A three-dimensional Voronoi polycrystal model with 125 grains was developed for analyzing the heterogeneous phenomena and microplasticity in polycrystalline solids. Using the crystal plasticity, finite element method, the role of the load modes in the response characteristics of severe plastic deformation was investigated. Among the tested load modes, uniaxial tension and plane compression are responsible for the presence of the shear band, while pure shear leads to uniform strain distribution, and simple shear leads to the concentration of deformation. The higher shear strain was achieved by torsion, followed by simple shear. At the start-up of the sliding system, torsion and pure shear have the strongest influence, while the effects of uniaxial compression and plane compression are relatively small. After experiencing the same strain, simple shear causes lower damage than torsion. In terms of the texture, after tensile strain, polycrystalline pure aluminum shows the texture of $<111>$//ND, after compression, the texture type is {110}//ND, and after torsion deformation, the texture type is $<111>$//TD. Under small strain, plane compression includes copper texture, brass texture, and S-texture. Under high strain, the {111} $<211>$ (annealed) texture was found in simple shear deformation. Experimental observation verified the high accuracy of the simulation results based on the excellent agreement between experiment and simulations for the stress–strain curve and texture evolution, and slip bands. Based on the principle of maximum cumulative plastic strain and minimum damage, simple shear is determined to be the optimal fine grain mode in the SPD process.

1. Introduction

Due to the great advantages of bulk nanomaterials and ultrafine-grained materials, severe plastic deformation methods (SPD) have received intense attention. In particular, the effect of deformation modes on structure evolution is considered to be the key basis for evaluating the effectiveness of SPD. Segal (Ref 1) has analyzed pure shear and simple shear and concluded that simple shear is the optimal deformation mode for the development of both high-angle boundaries and fine grains under monotonic loading and cross-loading. For this mode, different deformation techniques using simple shear processing are considered to be particularly suitable for equal channel angular pressing (ECAP) (Ref 2-4). Vinogradov et al. (Ref 5) employed either rolling or ECAP, i.e., pure shear or simple shear mode, to produce two types of specimens and compared their structures and mechanical behaviors. It was shown that both simple and pure shear deformation modes under the same equivalent strain eventually produce similar mechanical properties. In addition to simple shear and pure shear, some fundamental load modes such as tension, compression, torsion and plane strain or their combination contribute to the development of the structures and mechanical behaviors of the samples after severe plastic deformation. Li et al. (Ref 6, 7) used simulation and experiment to investigate the characteristics of combined tension-torsion (CCT) deformation, and the experimental results revealed that the microstructural evolution was consistent with the simulation results.

It is difficult to express the reorientation processes of individual grains after complex load processes in terms of simple empirical constitutive laws. Generally, experimental methods are applied, such as using electron backscatter diffraction patterns (Kikuchi patterns) from a scanning electron microscope. However, this is often neither practical nor scientifically rewarding because it provides a large amount of texture information that is usually unnecessary for predicting plastic anisotropy and the texture evolution. Various efficient numerical tools have been used to investigate the effect of load modes, among which the crystal plasticity finite element method (CPFEM) has recently been used in the simulation of fretting for detailed investigations of microplasticity of polycrystalline materials (Ref 8-10). The use of such methods is related to the need for greater insight into not only the macroscopic responses but also the local fields. Using CPFEM, considerable effort has been made to model polycrystalline materials and texture (Ref 11-13). Furthermore, there have been several studies focused on the microstructure evolution of a single crystal involving crystallographic slip patterns, plastic

Jinghui Li, Renhai Yu, Jintong Chen, and Mingya Zhang, School of Metallurgical Engineering, Anhui University of Technology, Ma'anshan 243002, China; Fuguo Li, School of Materials Science and Engineering, Northwestern Polytechnical University, Xi'an 710072, China; and Shan Liang, School of Innovation Education, Anhui University of Technology, Ma'anshan 243002, China. Contact e-mail: ljh0747@163.com.

zones and activated and dominated slip systems. For better construction of a polycrystalline model that is consistent with the actual grains, the 3D Voronoi diagram method was previously employed to discretize space at the grain level. This polycrystalline model was constructed and used for FEM analysis. Generally, two approaches were used to generate the initial orientation of the grains either as a random orientation distribution or as a distribution based on experimental observation. The 3D Voronoi model has been successfully applied in the simulations of tensile tests of polycrystalline aluminum samples (Ref 14-16). The simulation results show that the grain size has a significant effect on the deformation behavior, and the obtained simulated strain–stress relation was in good agreement with the experimental result. Zhang et al. (Ref 17) computationally investigated the contribution of dynamic compression and tension to the microdamage in polycrystalline ceramics using the Voronoi polycrystal model. The constitutive modeling considered crystal plasticity by basal slip, intergranular shear damage during compression and intergranular mode I cracking during tension.

This paper investigated the distributions of the stress, strain and slip systems in pure aluminum subjected to different load modes for a given appropriate value of the strain. The rate-dependent crystal plasticity theory and Voronoi polycrystalline model were adopted to quantitatively evaluate the influence of the load modes on the deformation behavior of the sample at the microscale. This model introduced the shape factor to control the shape, size and orientation of the grains. Through the Delaunay network, a Voronoi mosaic microstructure with a random orientation distribution was generated. The crystal plasticity was implemented in the ABAQUS finite element method (FEM) software combined with a user subroutine. The Taylor-type polycrystalline model and the hardening model considering the interaction of the sliding system were used in the finite element code to simulate the microshear band in pure polycrystalline aluminum.

2. Crystal Plasticity Model

2.1 Crystal Plasticity Constitutive Model

A strain-rate-dependent model was employed in this paper to represent the hardening of the rate-dependent properties of the used material. The model establishes the relationship between the decomposition shear stress . $\tau^{(\alpha)}$ and shear strain rate $\dot{\gamma}^{(\alpha)}$ as described by Eq 1:

$$\dot{\gamma}^{(\alpha)} = \dot{\gamma}_0^{(\alpha)} \mathrm{sgn}\left(\tau^{(\alpha)}\right) \left|\frac{\tau^{(\alpha)}}{\tau_c^{(\alpha)}}\right| \, for \, \tau^{(\alpha)} \geq \tau_c^{(\alpha)}$$

$$\dot{\gamma}^{(\alpha)} = 0 \, \text{for} \, \tau^{(\alpha)} < \tau_c^{(\alpha)} \tag{Eq 1}$$

$$\mathrm{sgn}(\tau^{(\alpha)}) = \begin{cases} 1 & \text{for } \tau^{(\alpha)} \geq 0 \\ -1 & \text{for } \tau^{(\alpha)} < 0 \end{cases}$$

where $\tau_c^{(\alpha)}$ is the critical shear stress value determining the start-up of the sliding system α. This value increases with deformation, reflecting the effect of work hardening and the difficulty of deformation, $\dot{\gamma}_0^{(\alpha)}$ is the reference shear strain rate corresponding to the shear stress that reaches its critical value, and n is the index describing the stress sensitivity of the slip system.

Here, a hardening model was established as given by Eq 2. This model fully considered the interaction between the slip systems and classified the slip systems. Different hardening parameters were selected for the interaction between the different slip systems to more accurately reflect the three hardening stages of the FCC crystal slip:

$$h_{\alpha\alpha} = \left\{ (h_0 - h_s)\mathrm{sech}^2\left[\frac{(h_0 - h_s)\gamma^{(\alpha)}}{\tau_1 - \tau_0}\right] + h_s \right\}\left\{ 1 + \sum_{\beta=1}^{N} f_{\alpha\beta} \tanh\left(\frac{\gamma^{(\beta)}}{\gamma_0}\right) \right\} \tag{Eq 2a}$$

$$h_{\alpha\beta} = qh_{\alpha\alpha}, \alpha \neq \beta \tag{Eq 2b}$$

where $h_{\alpha\beta}$ is the hardening modulus matrix, with $\alpha = \beta$ indicating self-hardening, while otherwise it means latent hardening. Generally, is the self-hardening coefficient, and $h_{\alpha\beta}(\alpha \neq \beta)$ is the latent hardening coefficient. q is the ratio of the latent hardening coefficient to the self-hardening coefficient, h_0 is the hardening modulus at the beginning of the yield, γ is the cumulative shear strain of the slip system, τ_0 is the initial critical shear stress, i.e., the initial strength of the slip system, τ_1 is the critical stress at the beginning of plastic flow, γ_0 is the reference value of the slip shear strain, h_s is the hardening modulus of the easy slip stage, and $f_{\alpha\beta}$ is the interaction coefficient between the slip system α and the slip system β, the value of which depends on the geometric relationship between the slip systems.

Kalidindi et al. proposed a fully implicit integration scheme, that is, two approaches to be used to set the time gradient: first, the stress, strain and state variables such as the strength, shear strain, and section shear stress of the current slip system are assumed, and then, the nonlinear incremental equation is expressed by the Newton–Raphson iterative method (Ref 18, 19).

(1) Using tangent modulus method to describe the time gradient

In the linear increment formula of nonlinear solution, the relationship between the shear strain and time increment is defined as:

$$\Delta\gamma^{(\alpha)} = \gamma^{(\alpha)}(t + \Delta t) - \gamma^{(\alpha)}(t) \tag{Eq 3}$$

Linear interpolation with Δt is described by:

$$\Delta\gamma^{(\alpha)} = \Delta t \left[(1 - \theta)\dot{\gamma}_t^{(\alpha)} + \theta\dot{\gamma}_{t+\Delta t}^{(\alpha)}\right] \tag{Eq 4}$$

where θ is the Euler time parameter ranging from 0.5 to 1.

The first-order Taylor expansion of $\dot{\gamma}_{t+\Delta t}^{(\alpha)}$ shows that:

$$\dot{\gamma}_{t+\Delta t}^{(\alpha)} \approx \dot{\gamma}_t^{(\alpha)} + \theta\frac{\partial\dot{\gamma}^{(\alpha)}}{\partial\tau^{(\alpha)}}\Delta\tau^{(\alpha)} + \theta\frac{\partial\dot{\gamma}^{(\alpha)}}{\partial g^{(\alpha)}}\Delta g^{(\alpha)} \tag{Eq 5}$$

Combining Eq 3 and 5 leads to the following equation:

$$\Delta\gamma^{(\alpha)} \approx \Delta t \left[\dot{\gamma}_t^{(\alpha)} + \theta\frac{\partial\dot{\gamma}^{(\alpha)}}{\partial\tau^{(\alpha)}}\Delta\tau^{(\alpha)} + \theta\frac{\partial\dot{\gamma}^{(\alpha)}}{\partial g^{(\alpha)}}\Delta g^{(\alpha)}\right] \tag{Eq 6}$$

Introducing the symmetric and asymmetric parts of the Schmid tensor of each slip system, $p_{ij}^{(\alpha)}$ and $\omega_{ij}^{(\alpha)}$ were represented as follows:

$$p_{ij}^{(\alpha)} = \frac{1}{2}\left(s_i^{(\alpha)}m_j^{(\alpha)} + s_j^{(\alpha)}m_i^{(\alpha)}\right)$$
$$\omega_{ij}^{(\alpha)} = \frac{1}{2}\left(s_i^{(\alpha)}m_j^{(\alpha)} - s_j^{(\alpha)}m_i^{(\alpha)}\right) \tag{Eq 7}$$

The incremental expression of the hardening function $\Delta g^{(\alpha)}$ is given by:

$$\Delta g^{(\alpha)} = \sum_\beta h_{\alpha\beta} \Delta\gamma^{(\beta)} \tag{Eq 8}$$

Therefore, the increment of the shear stress $\Delta\tau^{(\alpha)}$ in the section can be expressed as:

$$\Delta\tau^{(\alpha)} = \left[L_{ijl}\mu_{kl}^{(\alpha)} + \omega_{ik}^{(\alpha)}\sigma_{jk} + \omega_{jk}^{(\alpha)}\sigma_{ik} \right] \cdot \left[\Delta\varepsilon_{ij} - \sum_\beta \mu_{ij}^{(\alpha)}\Delta\gamma^{(\beta)} \right] \tag{Eq 9}$$

Considering the constitutive equation of material deformation in Eq 10, it is observed that the expression of synchronous rotation stress increment $\Delta\sigma_{ij}$ is given by Eq 11:

$$\hat{\sigma} = L : D - \sum_{\alpha=1}^{n} \left[L : P^{(\alpha)} + B^{(\alpha)} \right] \dot{\gamma}^{(\alpha)} \tag{Eq 10}$$

$$\Delta\sigma_{ij} = L_{ijk}\Delta\varepsilon_{kl} - \sigma_{ij}\Delta\varepsilon_{kk} - \sum_\alpha \left[L_{ijkl}\mu_{kl}^{(\alpha)} + \omega_{ik}^{(\alpha)}\sigma_{jk} + \omega_{jk}^{(\alpha)}\sigma_{ik} \right] \Delta\gamma^{(\alpha)} \tag{Eq 11}$$

For a given strain increment $\Delta\varepsilon_{ij}$, the shear strain increment can be uniquely determined by the following linear equation

$$\sum_\beta \left\{ \delta_{\alpha\beta} + \theta \frac{\partial\dot{\gamma}^{(\alpha)}}{\partial\tau^{(\alpha)}} \Delta\tau^{(\alpha)} \left[L_{ijkl}\mu_{kl}^{(\alpha)} + \omega_{ik}^{(\alpha)}\sigma_{jk} + \omega_{jk}^{(\alpha)}\sigma_{ik} \right] \mu_{ij}^{(\beta)} \right.$$
$$\left. - \theta\Delta t \frac{\partial\dot{\gamma}_t^{(\alpha)}}{\partial g^{(\alpha)}} h_{\alpha\beta} sign\left(\gamma_t^{(\beta)}\right) \right\}$$
$$\Delta\gamma^{(\beta)} = \dot{\gamma}_t^{(\alpha)}\Delta t + \theta\Delta t \frac{\partial\dot{\gamma}_t^{(\alpha)}}{\partial g^{(\alpha)}} \left[L_{ijkl}\mu_{kl}^{(\alpha)} + \omega_{ik}^{(\alpha)}\sigma_{jk} + \omega_{jk}^{(\alpha)}\sigma_{ik} \right] \Delta\varepsilon_{ij} \tag{Eq 12}$$

where $\delta_{\alpha\beta}$ is the Kronecker delta.

Given the increment of the slip shear stress $\Delta\gamma^{(\alpha)}$, other unknown values can be obtained by using the above formulas.

(2) Expression of nonlinear incremental formula by Newton–Raphson iteration

When the Taylor expansion of Eq 5 is canceled, all of the incremental equations remain unchanged except Eq 6, and the stress and state variables are calculated at the end of the time increment. The linear equation of shear strain $\Delta\gamma^{(\alpha)}$ is given by

$$\Delta\gamma^{(\alpha)} - (1-\theta)\Delta t\dot{\gamma}_t^{(\alpha)} - \theta\Delta t\dot{\gamma}_t^{(\alpha)} f^{(\alpha)}\left(\frac{\tau_t^{(\alpha)} + \Delta\tau^{(\alpha)}}{g_t^{(\alpha)} + \Delta g^{(\alpha)}} \right) = 0 \tag{Eq 13}$$

The material parameters of pure aluminum used in this paper are presented in Table 1. The parameters including the elastic properties, latent hardening and self-hardening of the slip

Table 1   Parameters of the interactions between the slip systems (Ref 21)

a1	a2	a3	a4	a5
1.75	1.75	1.75	2	2.25

systems are fitted from the experimental work of Zhang et al. (Ref 20).

3. Polycrystalline microstructure

Taking a cube with the dimensions of $1 \times 1 \times 1$ mm^3 as the space, a Voronoi diagram with 125 grains is established. First, the space is divided into 125 2a $\times$ 2b $\times$ 2c mm^3 hexahedra, as shown in Fig. 1(a). Then, in each isometric space, a certain rule is used to sow seeds. We use hexahedron (i, j, k) in Fig. 1(b) to illustrate this method: supposing that the central coordinate point of the hexahedron space is (x, y, z), then in the hexahedron, a small hexahedron is determined by points $(x - x, y - y, z - z)$ and $(x + x, y + y, z + z)$. In this small hexahedral space, the seeds are randomly distributed with $x = \alpha a$, $y = \beta b$, $z = \gamma c$ (α, β and γ are defined as shape control parameters), so that the positions of seed points in each partition area can be controlled by these three parameters (Table 2). The specific algorithm of generating three-dimensional Voronoi diagram with MATLAB is as follows:

(1) The values of the numbers of grains n_1, n_2, n_3 in three directions and the critical values of the shape control parameters α, β and γ and seed spacing are picked;
(2) The analysis area is divided into $n_1 \times n_2 \times n_3$ hexahedra, and the center coordinates of each hexahedron are calculated;
(3) In the first hexahedron, the position range is determined by the given shape control parameters α, β, γ and the coordinate of the center point of the hexahedron, and random seed 1 is generated;
(4) The seed point spacing between seed 1 and its adjacent hexahedron is calculated. If the spacing is greater than the given critical value, the seed is generated successfully and the algorithm proceeds to the next step. Otherwise, it will return to (3);
(5) Cycle through the remaining seeds according to the method in (3).

Figure 2 shows the three-dimensional Voronoi diagrams generated with different shape control parameters and composed of 125 cells. It can be observed that with increasing values of the shape control parameters, the degree of the irregularity of the cells in the Voronoi diagram increases significantly. The Voronoi diagram of $\alpha = \beta = \gamma = 0.5$ is in good agreement with experimental observations and therefore is selected as the simulated geometric model.

Generally, the orientation of metallic polycrystals tends to be scattered around one or some specific orientations in Eulerian space, where the value of the orientation distribution function represents the density near the specific orientation (Ref 22). The precise polycrystal model used in the finite element analysis is modeled strictly according to the Voronoi diagram. In this work, the coordinates of three-dimensional vertices of each grain were obtained based on MATLAB and implemented in ABAQUS in a Python routine. According to the mesh division of each grain, the interface of each grain is simplified accordingly. In the Python routine, the mesh size can be controlled by the control parameter M_s, as shown in Fig. 3. In the figure, the number of the grains is 125 and there are 125 random orientations, and the element type is C3D8I.
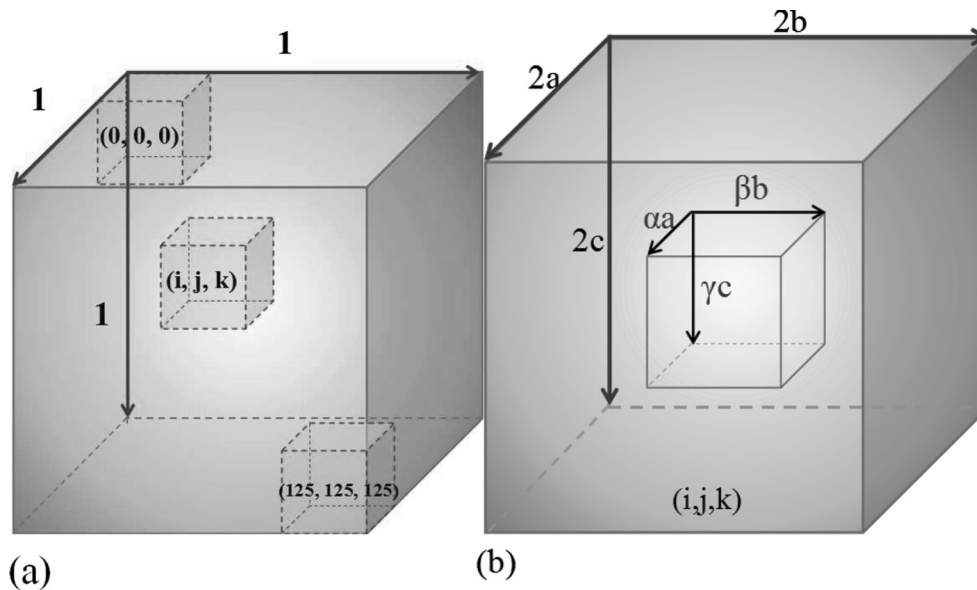
Fig. 1 Sketch map of seed point generation in 3D Voronoi diagram: (a) regional equal division; (b) cell species

Table 2 Parameters in the constitutive model (Ref [20])

n	$\dot{\gamma}_0$, 1/s	h_0, MPa	h_s, MPa	τ_1, MPa	τ_0, MPa	γ_0
300	0.0001	100	0.01	6.3	6	0.001

4. Results and Discussion

Figure 4 is a cloud chart of Mises stress distribution under different loading modes. It can be seen from the figure that there are obvious concave and convex phenomena on the surface of the model due to the inhomogeneous plastic deformation in the polycrystalline grains with different orientations. Moreover, the distribution of the stress and strain in grains is not uniform, with a clear stress concentration around the grain boundaries. This is due to the preferential plastic deformation of the grains under external loading on the slip surface with the minimum critical shear stress. Based on the overall stress distribution of the analysis model, the loading mode has a strong influence on the stress distribution in the specimen. For uniaxial tension, compression and simple shear deformation, the stress distribution inside the specimen is relatively uniform, while the stress of the torsion and pure shear deformation specimen is relatively large, and the distribution is uneven.

Figure 5 shows the change curve of the Mises stress and shear stress with deformation (time) of the selected element. It is observed from Fig. 5(a) that the Mises stress of torsion deformation is significantly higher than that of other deformation modes, which is followed by the Mises stress of simple shear deformation. Thus, high Mises stress can be produced rapidly in grains during torsion deformation. In the process of large plastic deformation, the grain refinement is first initiated by the slip system under the action of shear stress and then stops during the sliding process, leading to the appearance of local stress concentration and grain refinement. Therefore, Fig. 5(b) shows the shear stress distribution of the selected

element under different loading modes. The analysis shows that the shear stress is the greatest (approximately 110 MPa) under torsion and simple shear deformation modes, while the shear stress is 85 MPa under pure shear. Torsion deformation and simple shear deformation can also initiate the slip system during the deformation process, so as to achieve grain refinement.

Figure 6 shows the distribution of the maximum principal strain for the strain of 0.1. Similar to the equivalent stress distribution, the maximum principal strain also shows an obvious nonuniform distribution with a gradient in the grain. Some grains show heavy deformation, and the grain boundary also displays large deformation that will hinder the deformation of the adjacent grains. Due to the differences in their grain orientations, the degree of deformation will be different for each grain. Comparison of the strain distribution nephograms under different loading modes shows that shear bands can form in local areas under the uniaxial tension and plane compression deformation. As shown by the red lines in Fig. 6(a) and (d), the shear bands have an angle of 45° along the direction of tension or compression. However, under other loading modes, such obvious shear bands cannot be formed. Comprehensive analysis shows that the compression strain is small and uniformly distributed, while it is the largest and unevenly distributed after torsion. The strain distribution produced by pure shear is more uniform. Simple shear gives rise to a strain concentration in the local area of grains, and the strain difference between the adjacent grains is large.
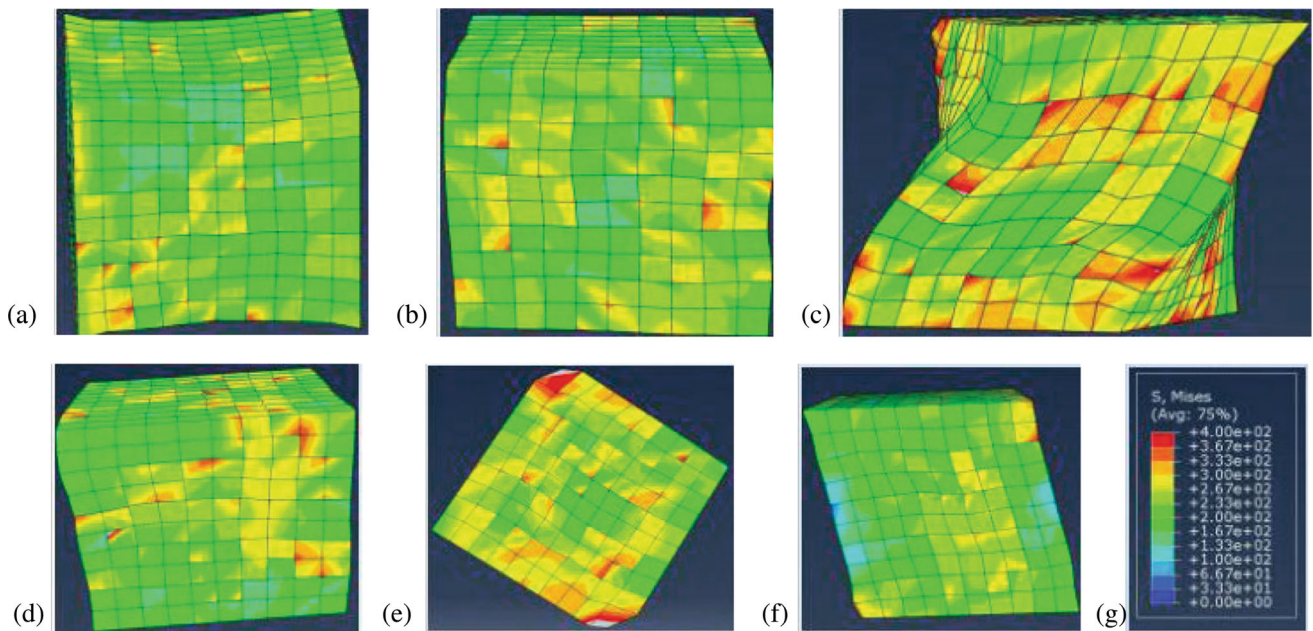
Figure 7 shows the results for the accumulated shear strain of the selected element under different loading modes. It is observed that the highest cumulative shear strain is obtained for
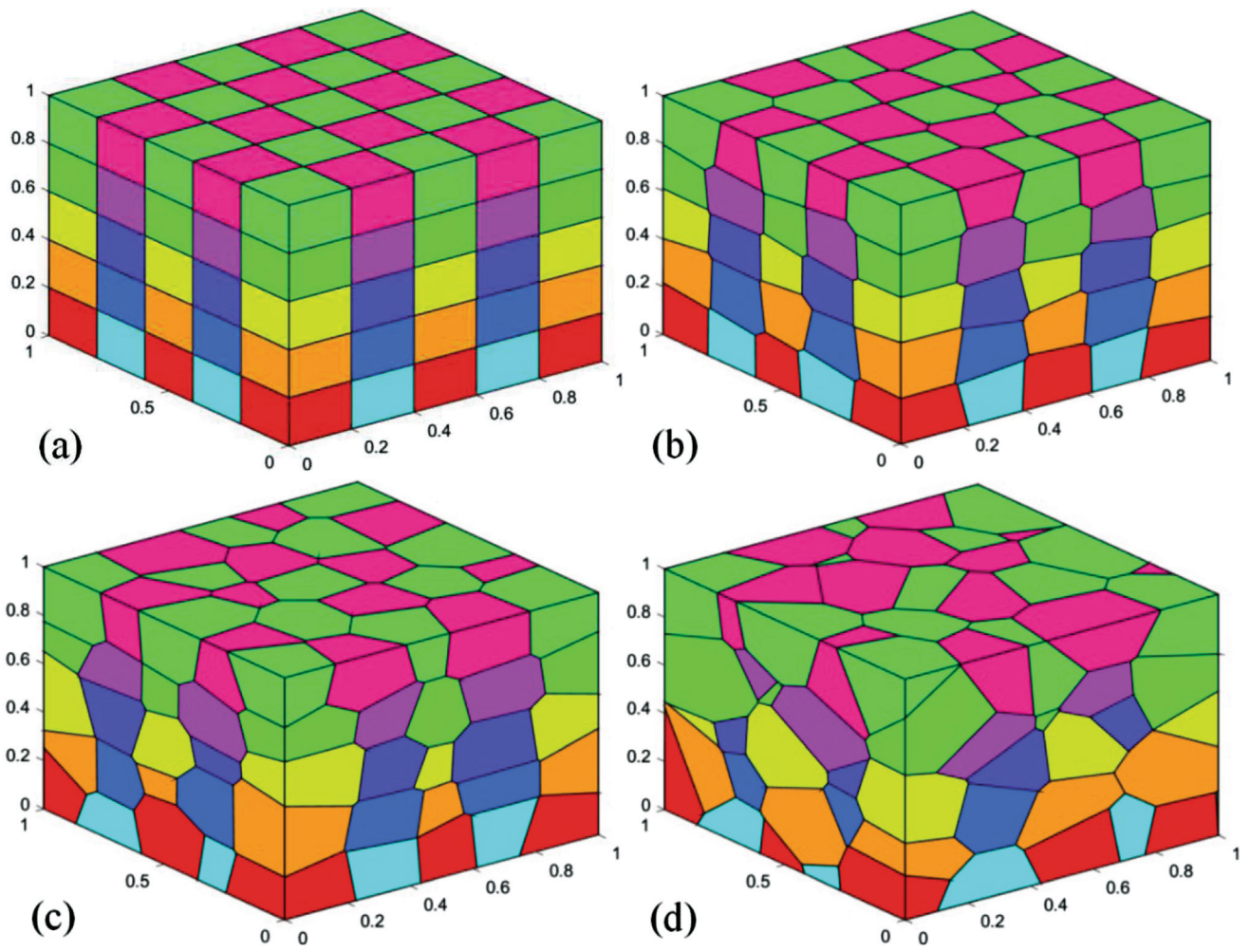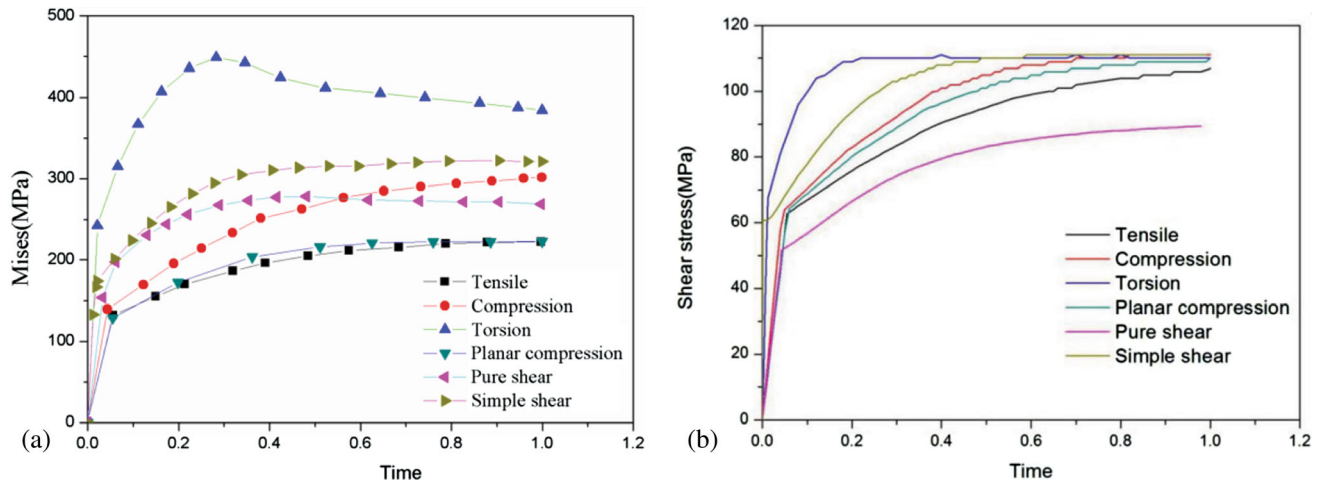
Fig. 2 3D Voronoi graphs with different shape control factors ($\alpha = \beta = \gamma$): (a) 0; (b) 0.25; (c) 0.5; (d) 1
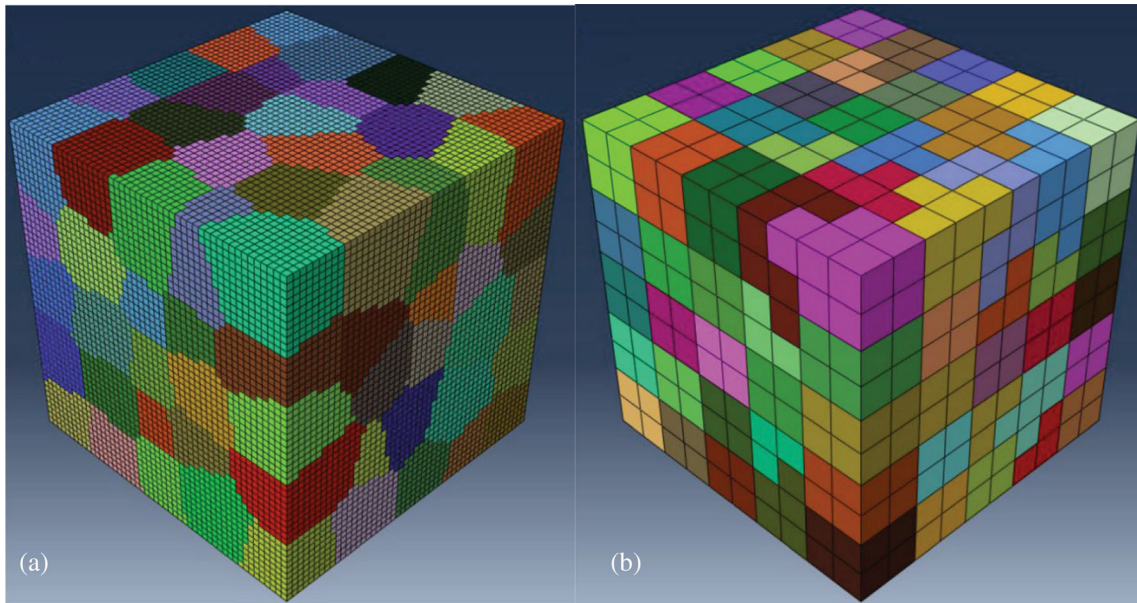
Fig. 3 Simplified polycrystalline models controlled by different mesh sizes: (a) $M_s = 0.02$; (b) $M_s = 0.1$

Fig. 4 Stress distribution nephogram: (a) uniaxial tension; (b) uniaxial compression; (c) uniaxial torsion; (d) planar compression; (e) pure shear; (f) simple shear; (g) legend
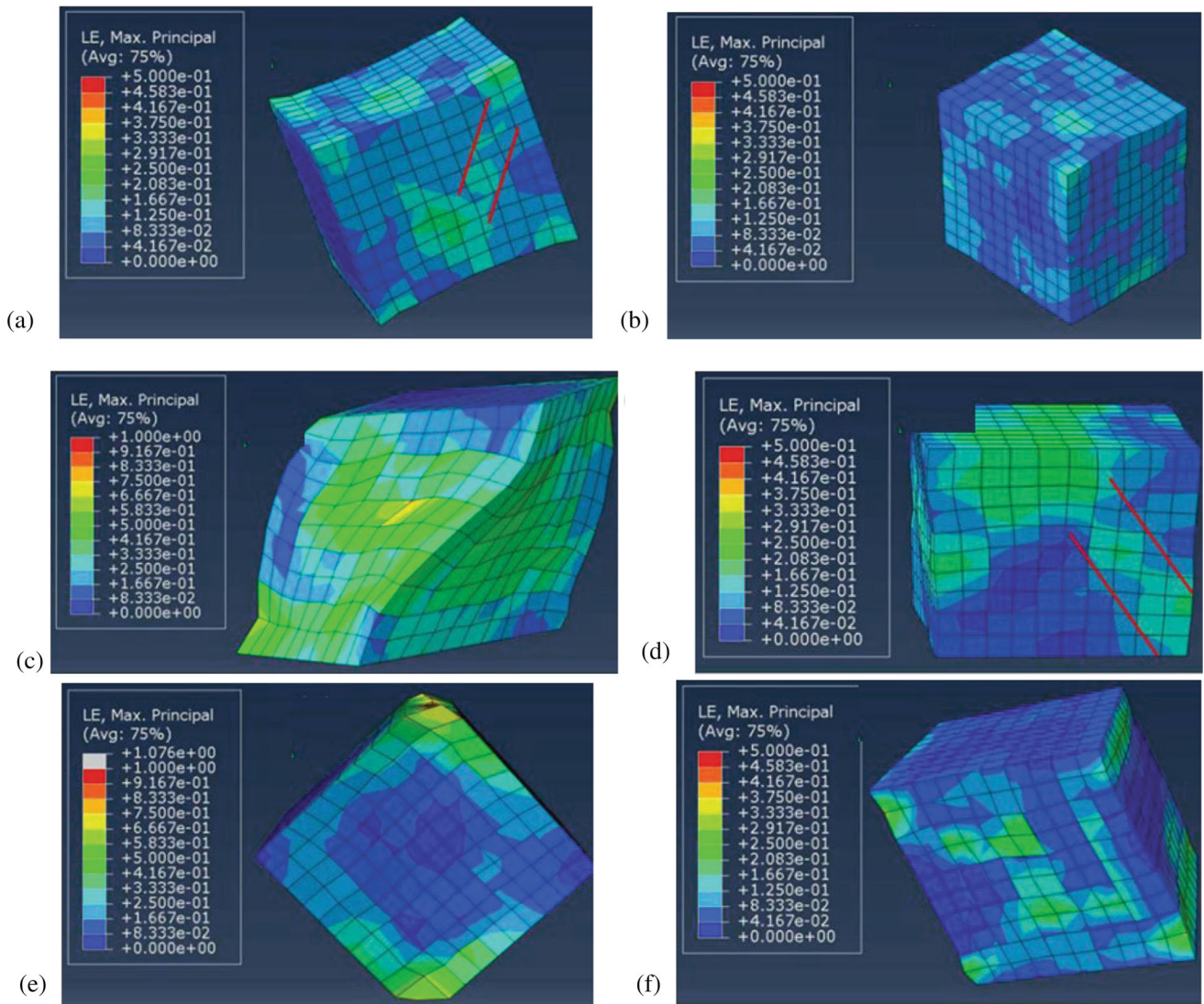

Fig. 5 Variation trend of stress with simulated time under different loading modes: (a) Mises stress; (b) shear stress

the torsion deformation, followed by simple shear. The accumulated shear strain is smaller under other loading modes. For the displacement of 0.1, i.e., the time is 1.0, the torsion cumulative shear strain is approximately 1.2, and the simple shear is approximately 0.5. The accumulated shear stress of the other four loading methods is relatively small due to the shear stress component of the grains during the deformation and is basically consistent with the analysis results presented in Fig. 6.

However, it is not comprehensive to judge the optimal grain refinement mechanism only from the cumulative shear strain in Fig. 7. It is still necessary to consider the evolution of damage presented during deformation process. Figure 8 shows the variation trend of damage in terms of six-load condition. As seen in Fig. 8, suffering the same strain, the values of cumulative damage under compression and torsion are the largest, while the least for pure shear and simple shear. In addition, torsion deformation can accumulate damage in a short

time; this is not conducive to the continuation of straining. In consideration of the principle, namely maximum plastic strain accumulation and minimum damage, the torsion deformation cannot be regarded as the optimal fine-grained mode of SPD deformation, while the simple shear can be taken as the optimal one.

According to the classical crystal plasticity theory, the presence of plastic deformation is the driving force for the start-up and sliding of different slip systems, but when the crystal undergoes plastic deformation, only some slip systems can be activated. To elucidate the influence of the deformation mode on the grain sliding system, specific cellular grains were selected for analysis. The normal and tangential direction of the sliding surface is characterized by SDV37-39 and SDV73-75, respectively, as shown in Fig. 9. It is observed that there is a relationship between the initiation of the slip system in the grains and the macrostress distribution, and the initiation of
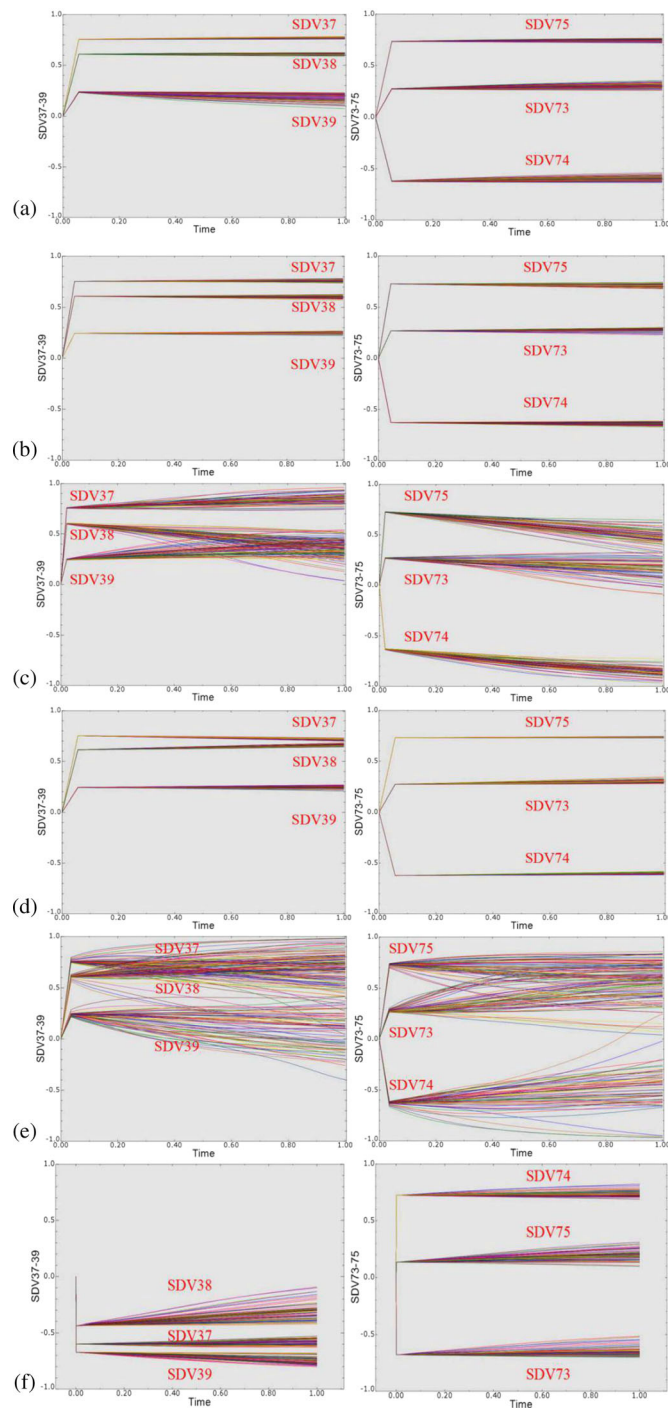
Fig. 6 Strain distribution nephogram: (a) uniaxial tension; (b) uniaxial compression; (c) uniaxial torsion; (d) planar compression; (e) pure shear; (f) simple shear
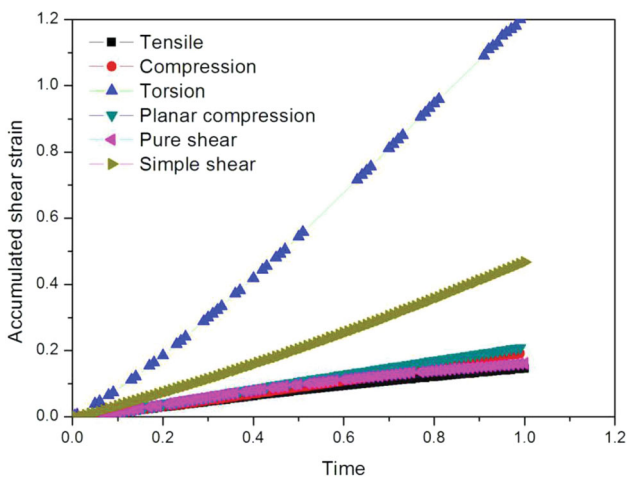
Fig. 7 Variation trend of accumulated shear strain with simulated time under different loading modes of the selected element
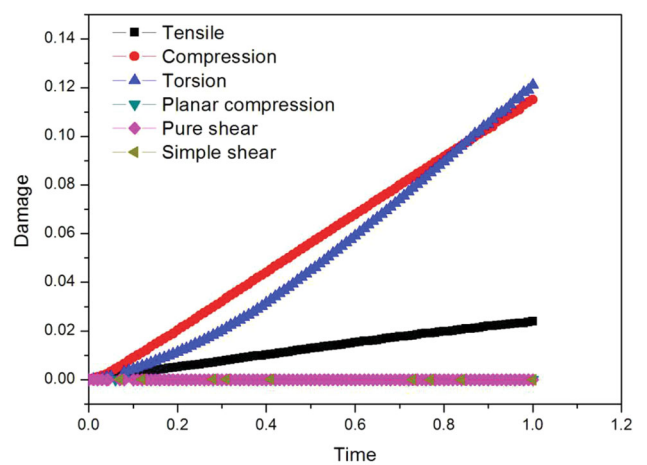
Fig. 8 Variation trend of accumulated damage with simulated time under different loading modes of the selected element
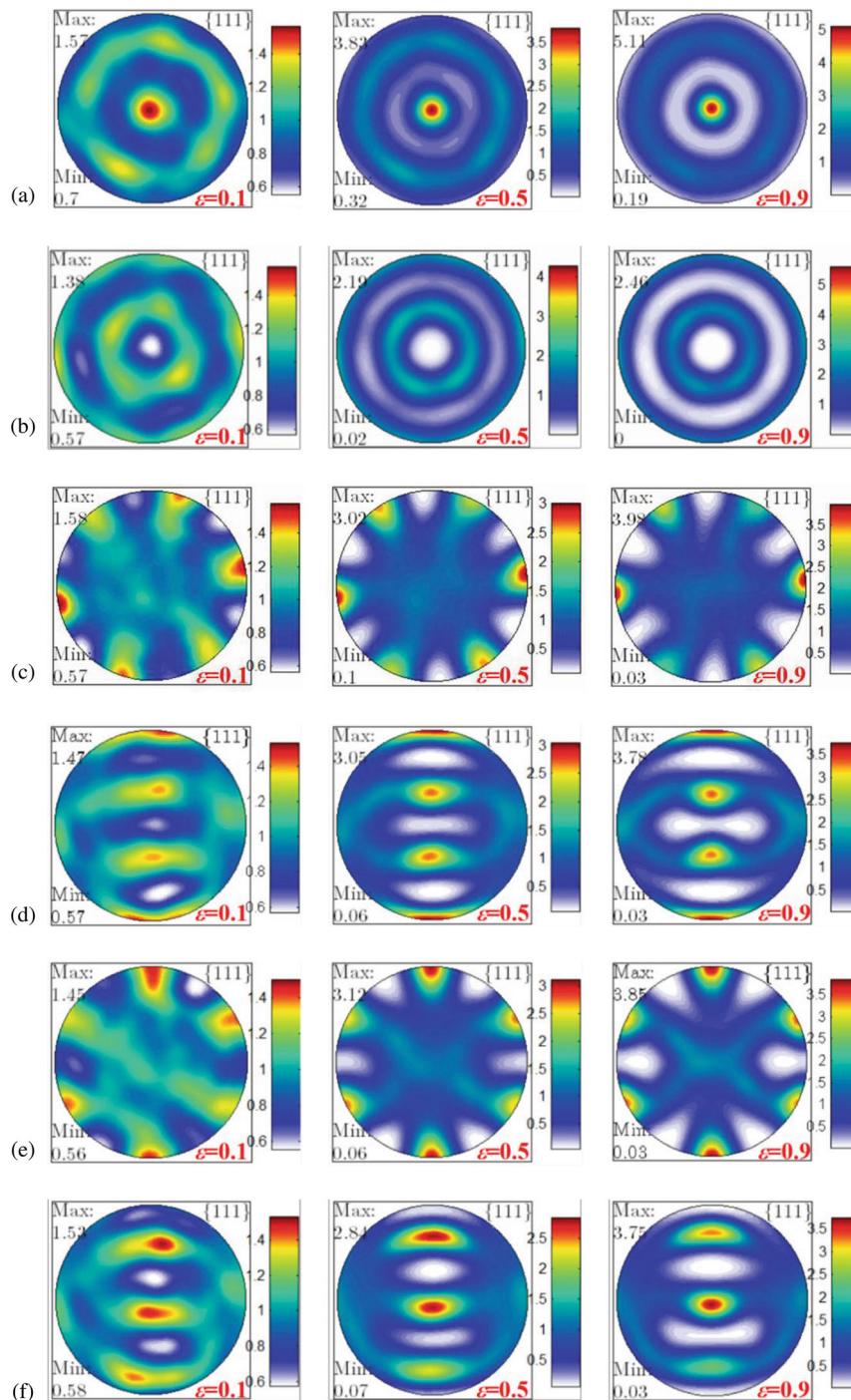
Fig. 9 Time-dependent trend of slip system of all nodes of the selected element: (a) uniaxial tension; (b) uniaxial compression; (c) uniaxial torsion; (d) planar compression; (e) pure shear; (f) simple shear

different slip systems in the grains also presents an uneven distribution. Moreover, as the plastic deformation became more intense, the sliding system initiated, but the response of the start of the sliding system to the loading mode varied strongly depending on the deformation mode, with torsion deformation and pure shear deformation exerting the strongest influence on the start of the sliding system, and uniaxial compression and plane compression exerting the least influence. In addition, the starting conditions of the simple shear slip system are different from those of other modes in that the SDV37-39 is negative.

The pole diagram from different loads is obtained in Fig. 10. For most face-centered cubic (FCC) metals, the slip surfaces are mostly {111} surfaces, and therefore the {111} polar diagram is often used to characterize the texture of FCC metals. The evolution of texture under different load modes of the strain ranging from 0.1 to 0.9 is obtained by simulation. The ordinate direction with the center point as the origin is RD direction, and the abscissa to the right is TD direction.

From the result in Fig. 10, the six deformation modes can make the texture tend to concentrate. With the increase in

Fig. 10 {111} polar diagram of polycrystalline pure aluminum under different loading modes: (a) uniaxial tension; (b) uniaxial compression; (c) uniaxial torsion; (d) planar compression; (e) pure shear; (f) simple shear

deformation degree, the grain orientation is more concentrated and the texture is stronger. After 0.9 tensile strain, polycrystalline pure aluminum shows the texture in the direction of $<111>$//ND; after compression, the sample shows the texture in the direction of {110}//ND; and after torsional deformation, the texture type is $<111>$//TD. Compared with the texture in the strain of 0.1, the texture in the strain of 0.9 rotates anticlockwise in the direction of ND by 10°; the plane compression strain includes copper texture and brass texture in the low strain. Under high strain, the texture is mainly copper

type; pure shear deformation texture is copper type; and simple shear deformation texture is {111} $<211>$ (annealed) texture.

5. Experimental Verification

Prior to the deformation, all of the samples were annealed in a furnace. The samples were heated to 450 °C for 2 h and then were cooled in the furnace. For calibration and verification of the model, we characterized the responses of the above six load

modes to the strain of 0.1 for a polycrystalline pure aluminum with 99.9 wt.% purity to estimate the stress–strain curve, texture evolution and the slip bands of the samples. The tensile specimen was plate-shaped with a length and width of 100 mm and 20 mm, respectively. The height and diameter of the uniaxial compression specimen were 12 mm and 8 mm, respectively. For planar compression, the sample was constrained in the transverse direction. The sample dimensions were approximately $10 \times 10 \times 6$ mm^3, and the test details are described in (Ref 23). These three tests were carried out using an Instron 3382 Material Testing Machine (MTS). Cylindrical samples with a diameter and length of 8 mm and 44 mm, respectively, were deformed in the torsion achieved in wire torsion testing machine as described in the literature (Ref 24). The simple shear and pure shear experiments were carried out using variable angle fixture, and a detailed description of the procedure is provided in the literature (Ref 25, 26).

Figure 11 shows the experimental and simulated stress vs. strain curves for the three load tests at the strain of 0.1. As observed from Fig. 10, a good agreement between the predicted stress–strain curve and the experimental stress–strain curve was obtained, with a particularly good agreement in the initial yield range. The experimental observation also confirms the hardening trend obtained by the CPFEM model of a motivated

hardening dependence in polycrystals based on their slip systems. Generally, slip system hardening is achieved through statistically stored dislocations, and the process can be described by some equations that capture the influence of the self- and latent hardening employed in the present study. For uniaxial compression, as the strain increases, the analysis shows much more hardening than that observed in the experiment owing to the contributions of the additional damage or failure mechanisms within the material. However, the opposite results were found for planar compression subjected to the constraints from three surfaces that led to a reduced probability of damage or failure.

The (1 1 1) pole figures for pure aluminum deformed by four different modes obtained experimentally using electron backscatter diffraction (EBSD) are shown in Fig. 12. It is observed that similar to the simulated results, the pure aluminum samples after 10% reduction also show very strong orientation dispersion displaying good agreement between the simulated and the symmetrized experimental pole figures. This comparison shows that the CPFEM model underestimates the texture spread for the FCC crystal. The texture of the experimental tension sample is slightly different from that in the simulated tension sample. The pole figure morphology for the uniaxial compression is characterized by the clustering of
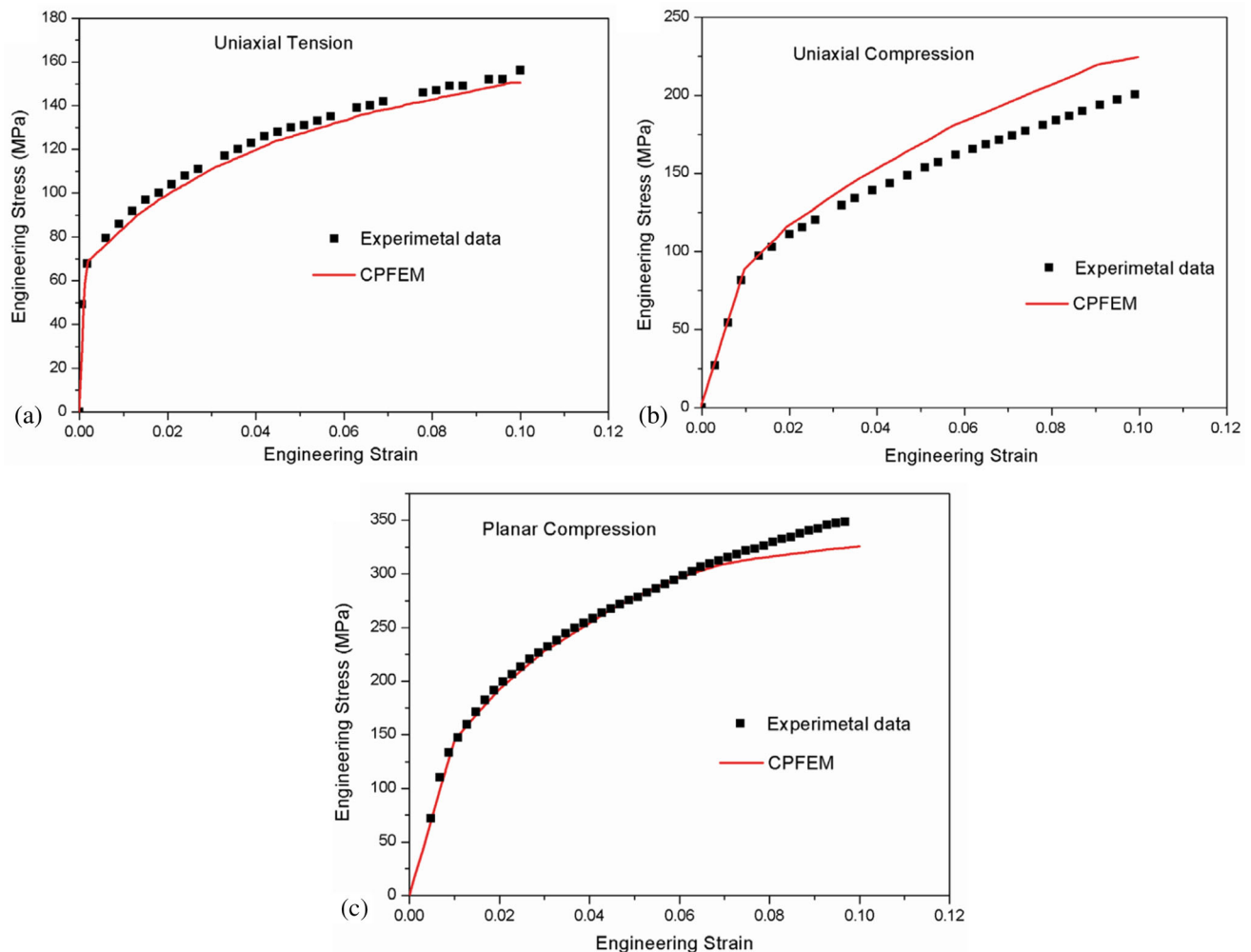
Fig. 11 Material response based on simulated and experimental results of pure aluminum subjected to: (a) uniaxial tension; (b) uniaxial compression; (c) planar compression
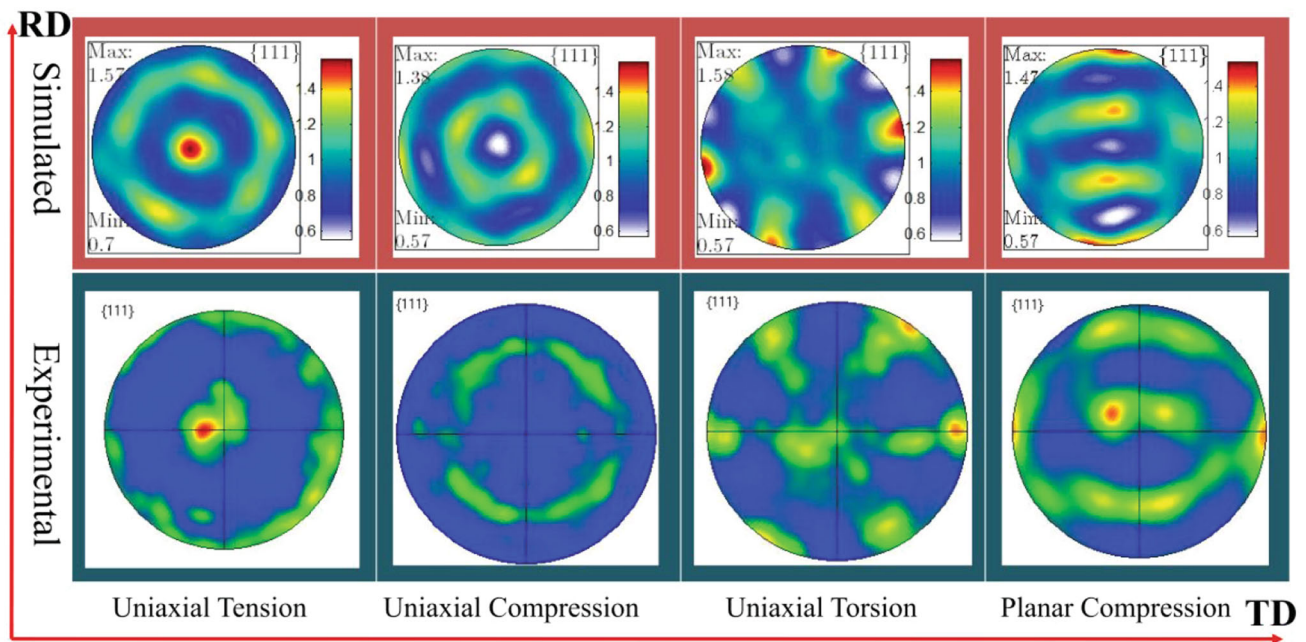
Fig. 12 Experimental and simulated {111} polar diagram of pure aluminum under four loading modes

the orientations into "4 lobes" around the center region. Another important phenomenon is the relatively weaker texture obtained experimentally for the uniaxial compression sample compared to that in the simulation, which is attributed to the discontinuity in the experimental bulk material with many micropores. During the compression process, the imposed strain will be consumed, particularly for small strain. On the other hand, in both simulation and experiment, the texture of planar compression is characterized by the presence of the copper and brass texture components. Although the CPFEM simulations do not fully capture the microstructural details, they do provide a possible deformation mechanism that will eventually lead to the simulated texture. Several previous studies have concluded that more accurate simulated texture with better agreement with the experimental results is obtained for a greater number of grains and denser simulation mesh (Ref 27–32).

Some special phenomena were observed in the experiment, particularly for uniaxial tension, as shown in Fig. 13. After tension, coarse grains such as Grain 1 and Grain 2 elongated and a large number of slip bands appeared inside the grains marked by the yellow rectangular frame in Fig. 13. The macroscopic fracture morphology shows that the fracture starts at the edge of the sample and develops through the grain, and the microscopic fracture presents the transformation process from the brittle edge of the pure aluminum sample to tough center of the sample. The initiation and proliferation of the slip system prior to the fracture were observed, as predicted by the simulation results in Fig. 9. In the preliminary CPFEM that used self- and latent hardening of the microstructures, the development of the slipping system is responsible for the macrocrack observed at the slipping system (see the small yellow rectangular frame in Fig. 13). The presence of dense slip bands also shows that an increase in the average number of active slip systems was confirmed in both the experiment and simulation.

6. Conclusions

A three-dimensional Voronoi polycrystalline geometric model is established, and the combination of crystal plasticity finite element and damage model is realized by simulations carried out using ABAQUS combined with a Python routine. The stress distribution, strain distribution, slip system start-up, deformation damage and texture evolution under different loading modes are predicted and verified.

(1) In the processes of uniaxial tension, compression and simple shear, the stress distribution is relatively uniform, while in the uniaxial torsion and pure shear deformation, the stress is large and is unevenly distributed. Uniaxial tension and plane compression easily produce local deformation shear bands, and this phenomenon was verified by experimental observation for the uniaxial tension test of coarse pure aluminum. Pure shear produces a more uniform deformation strain, and simple shear leads to the concentration of the deformation in the local area. The cumulative shear strain of torsion deformation is the largest, followed by that of simple shear.

(2) Torsion deformation and pure shear deformation have the strongest effect on the start-up of the sliding system, while uniaxial compression and plane compression have relatively small influence on the sliding system.

(3) After the same strain for simulation, the cumulative damage of plane compression and torsion is the largest, while pure shear and simple shear damage are the least. For the stress–strain curves under the same strain, it was found that the experimental observation and the simulation results show excellent agreement, verifying the accuracy of the simulation.

(4) After tensile strain, pure aluminum shows the texture of $<111>$//ND, while after compression, the texture type is {110}//ND, and after torsion deformation, the texture type is $<111>$//TD. Under low strain, plane compres-
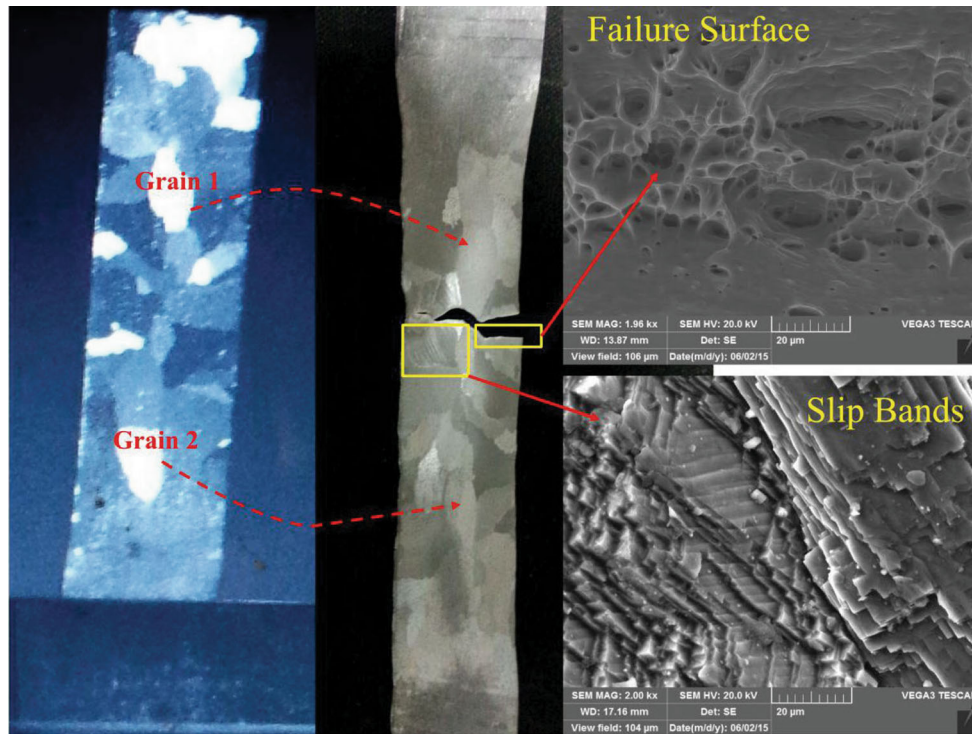
Fig. 13 Fracture and slip bands in pure aluminum under uniaxial tension

sion deformation includes copper texture, brass texture and S-texture. Under high strain, the texture is mainly copper type, and after pure shear, the texture is copper type, while $\{111\} <211>$ (annealed) texture is obtained for simple shear. Experimental observations of the texture of the sample are in good agreement with the simulated results.

In conclusion, based on the principle of maximum accumulated plastic strain and minimum damage, it can be concluded that simple shear is the optimal fine-grain mode in the SPD process.

Acknowledgments

References

1. V.M. Segal, Severe Plastic Deformation: Simple Shear Versus Pure Shear, *Mater. Sci. Eng. A*, 2002, **338**(1–2), p 331–344
2. A. Shan, I.G. Moon, H.S. Ko and J.W. Park, Direct Observation of Shear Deformation During Equal Channel Angular Pressing of Pure Aluminum, *Scr. Mater.*, 1999, **41**(4), p 353–357
3. M. Furukawa, Z. Horita and T.G. Langdon, Microstructures of Aluminum and Copper Single Crystals Processed by Equal-Channel Angular Pressing, *Mater. Sci. Forum*, 2010, **638–642**, p 1946–1951
4. R. Venkatraman, S. Raghuraman and R.R. Mohan, Modeling and Analysis on Deformation Behavior for AA 6061 through Equal Channel Angular Pressing Die, *Commun. Comput. Inf. Sci.*, 2012, **330**, p 520–525
5. A. Vinogradov, S. Yasuoka, S. Hashimoto, On the Effect of Deformation Mode on Fatigue: Simple Shear vs. Pure Shear, Materials Science Forum, 2008, Trans Tech Publ, p 797–802
6. J. Li, F. Li, M.Z. Hussain, C. Wang and L. Wang, Micro-structural Evolution Subjected to Combined Tension-Torsion Deformation for Pure Copper, *Mater. Sci. Eng. A*, 2014, **610**, p 181–187
7. J. Li, F. Li, C. Zhao, H. Chen, X. Ma and J. Li, Experimental Study on Pure Copper Subjected to Different Severe Plastic Deformation Modes, *Mater. Sci. Eng. A*, 2016, **656**, p 142–150
8. S.H. Choi, D.H. Kim, S.S. Park and B.S. You, Simulation of Stress Concentration in Mg Alloys Using the Crystal Plasticity Finite Element Method, *Acta Mater.*, 2010, **58**(1), p 320–329
9. A.K. Kanjarla, P.V. Houtte and L. Delannay, Assessment of Plastic Heterogeneity in Grain Interaction Models Using Crystal Plasticity Finite Element Method, *Int. J. Plast*, 2010, **26**(8), p 1220–1233
10. Y. Liang, S. Jiang, Y. Zhang, Y. Zhao, S. Dong and C. Zhao, Deformation Heterogeneity and Texture Evolution of NiTiFe Shape Memory Alloy Under Uniaxial Compression Based on Crystal Plasticity Finite Element Method, *J. Mater. Eng. Perform.*, 2017, **26**(6), p 2671–2682
11. Y.S. Choi, M.A. Groeber, P.A. Shade, T.J. Turner, J.C. Schuren, D.M. Dimiduk, M.D. Uchic and A.D. Rollett, Crystal Plasticity Finite Element Method Simulations for a Polycrystalline Ni Micro-Specimen Deformed in Tension, *Metall. Mater. Trans. A*, 2014, **45**(13), p 6352–6359
12. D.K. Kim, J. Kim, W. Park, H.W. Lee, Y.T. Im and Y.S. Lee, Three-Dimensional Crystal Plasticity Finite Element Analysis of Microstructure and Texture Evolution During Channel Die Compression of IF Steel, *Comput. Mater. Sci.*, 2015, **100**, p 52–60
13. H.K. Ji, M.G. Lee, J.H. Kang, C.S. Oh and F. Barlat, Crystal Plasticity Finite Element Analysis of Ferritic Stainless Steel for Sheet Formability Prediction, *Int. J. Plast*, 2017, **93**, p 26–45
14. O. Ozhoga-Maslovskaja, K. Naumenko, H. Altenbach and O. Prygorniev, Micromechanical Simulation of Grain Boundary Cavitation in Copper Considering Non-proportional Loading, *Comput. Mater. Sci.*, 2015, **96**, p 178–184
15. P. Zhang, M. Karimpour, D. Balint, J. Lin and D. Farrugia, A Controlled Poisson Voronoi Tessellation for Grain and Cohesive

Boundary Generation Applied to Crystal Plasticity Analysis, *Comput. Mater. Sci.*, 2012, **64**, p 84–89

16. S.I. Liang-Ying, L.Ü. Cheng, K. Tieu and X.H. Liu, Simulation of Polycrystalline Aluminum Tensile Test with Crystal Plasticity Finite Element Method, *Trans. Nonferrous Met. Soc. China*, 2007, **17**(6), p 1412–1416

17. K.S. Zhang, D. Zhang, R. Feng and M.S. Wu, Microdamage in Polycrystalline Ceramics Under Dynamic Compression and Tension, *J. Appl. Phys.*, 2005, **98**(2), p 79

18. J. Alcalá, O. Casals and J. Očenášek, Micromechanics of Pyramidal Indentation in fcc Metals: Single Crystal Plasticity Finite Element Analysis, *J. Mech. Phys. Solids*, 2008, **56**(11), p 3277–3303

19. P.T. Wei, C. Lu, K. Tieu, G.Y. Deng and J. Zhang, Modelling of Texture Evolution in High Pressure Torsion by Crystal Plasticity Finite Element Method, *Appl. Mech. Mater.*, 2015, **764–765**, p 56–60

20. K. Zhang, B. Holmedal, O.S. Hopperstad, S. Dumoulin, J. Gawad, A. Van Bael and P. Van Houtte, Multi-level Modelling of Mechanical Anisotropy of Commercial Pure Aluminium Plate: Crystal Plasticity Models, Advanced Yield Functions and Parameter Identification, *Int. J. Plast.*, 2015, **66**, p 3–30

21. L.Y. Si, C. Lu, N.N. Huynh, A.K. Tieu and X.H. Liu, Simulation of Rolling Behaviour of Cubic Oriented al Single Crystal with Crystal Plasticity FEM, *J. Mater. Process. Technol.*, 2008, **201**(1–3), p 79–84

22. H. Ritz, P. Dawson and T. Marin, Analyzing the Orientation Dependence of Stresses in Polycrystals Using Vertices of the Single Crystal Yield Surface and Crystallographic Fibers of Orientation Space, *J. Mech. Phys. Solids*, 2010, **58**(1), p 54–72

23. D. Raabe and F. Roters, Using Texture Components in Crystal Plasticity Finite Element Simulations, *Int. J. Plast.*, 2004, **20**(3), p 339–361

24. H. Li, A. Oechsner, D. Wei, G. Ni and Z. Jiang, Crystal Plasticity Finite Element Modelling of the Effect of Friction on Surface Asperity Flattening in Cold Uniaxial Planar Compression, *Appl. Surf. Sci.*, 2015, **359**(30), p 236–244

25. C. Wang, F. Li, L. Wei, Y. Yang and J. Dong, Experimental Microindentation of Pure Copper Subjected to Severe Plastic Deformation by Combined Tension-Torsion, *Mater. Ence Eng. A*, 2013, **571**(1), p 95–102

26. J. Cao, F. Li, X. Ma and Z. Sun, A Modified Elliptical Fracture Criterion to Predict Fracture Forming Limit Diagrams for Sheet Metals, *J. Mater. Process. Technol.*, 2018, **252**, p 116–127

27. J. Cao, F. Li, Z. Sun and X. Ma, Study of Fracture Behavior for Anisotropic 7050–T7451 High-Strength Aluminum Alloy Plate, *Int. J. Mech. Sci.*, 2017, **128**, p 445–458

28. H.F. Alharbi and S.R. Kalidindi, Crystal Plasticity Finite Element Simulations Using a Database of Discrete Fourier Transforms, *Int. J. Plast.*, 2015, **66**, p 71–84

29. O. Diard, S. Leclercq, G. Rousselier and G. Cailletaud, Evaluation of Finite Element Based Analysis of 3D Multicrystalline Aggregates Plasticity: Application to Crystal Plasticity Model Identification and the Study of Stress and Strain Fields Near Grain Boundaries, *Int. J. Plast.*, 2005, **21**(4), p 691–722

30. U. Borg, A Strain Gradient Crystal Plasticity Analysis of Grain Size Effects in Polycrystals, *Eur. J. Mech. A Solids*, 2007, **26**(2), p 313–324

31. G. Venkatramani, S. Ghosh and M. Mills, A Size-Dependent Crystal Plasticity Finite-Element Model for Creep and Load Shedding in Polycrystalline Titanium Alloys, *Acta Mater.*, 2007, **55**(11), p 3971–3986

32. X. Lu, X. Zhang, M. Shi, F. Roters, G. Kang and D. Raabe, Dislocation Mechanism Based Size-Dependent Crystal Plasticity Modeling and Simulation of Gradient Nano-grained Copper, *Int. J. Plast.*, 2019, **113**(2), p 52–73